

# A Novel Triad Twisted String Actuator for Controlling a Two Degrees of Freedom Joint: Design and Experimental Validation

Damian Crosby *Graduate Student Member, IEEE*, Joaquin Carrasco *Member, IEEE*, William Heath *Member, IEEE*, and Andrew Weightman

**Abstract**—Actuated universal joints, or equivalent joint systems, are found in a number of robotic applications, in particular mobile snake robots, snake-arm robots and robotic tails. Such joints use a variety of actuation methods, including direct drive motors, linear screw drives, cable based systems, and hydraulics/pneumatics. In this paper the authors present a novel design for a mechanism that utilises the twisted string actuator in an antagonistic triad to actuate the universal joint, using orientation sensors and load cells to create a robust cascading closed loop control system. This design realises a light, compact, high-performance actuation system that avoids the extra mass and hardware complexity that alternative actuation methods present, with the additional challenge of nonlinearity. The authors were able to develop a closed loop control system that could track a universal joint orientation setpoint to within  $\pm 1.8^\circ$  within a  $\pm 11^\circ$  range for a single axis and  $\pm 6^\circ$  range for dual axis.

**Index Terms**—???

## I. INTRODUCTION

Actuated universal joint (AUJ) mechanisms are found in a wide range of robotic applications, such as confined space inspection using continuum robots [1], highly manoeuvrable mobile snake robots [2], and biomimetic robot tails for stability [3]. Mobile snake robots must usually incorporate electric actuators inline with their joints. This results in an AUJ having to shift the mass of the follower segments and all the actuators inside the follower segments, which results in high torque requirements. Continuum robots and robotic tails can reduce the mass and size of the AUJ by moving their actuators away from the AUJs and use cables to transfer the force to the joints, or use hydraulic or pneumatic actuators which tend to be lighter than equivalent electric motors. This comes at the expense of increased mass and bulk at the base of the arm or tail.

D. Crosby, J. Carrasco and W. Heath are with the Department of Electrical and Electronic Engineering, School of Engineering, Faculty of Science and Engineering, The University of Manchester, Manchester, United Kingdom.

A. Weightman is with the Department of Mechanical, Aerospace and Civil Engineering, School of Engineering, Faculty of Science and Engineering, The University of Manchester, Manchester, United Kingdom.

First developed by Würtz *et al.* [4] in 2010, the TSA uses two or more strings between two fixtures as a linear actuator. When one fixture is rotated (typically by an electric motor), the looped string twists into a helix, decreasing the distance between them. TSA actuators have been used for a hand orthosis [5], elbow joint [6] and foldable robot arm [7] among other functions.

The primary advantage of TSA over similar linear actuators such as a leadscrew is the reduction (lower velocity, higher torque) the TSA provides is not proportional to the mass of the actuator, in fact it is slightly inversely proportional. Generally, to increase the reduction in an actuator requires the addition of a gearbox which increases mass, but in the case of the TSA, by decreasing the string cross-section radius, the reduction increases given a constant unwound length and motor angle, resulting in a greater reduction with no increase, or even a slight decrease, in actuator mass.

While the reduction in a leadscrew can be increased by decreasing the lead on the thread, which also has no increase in mass, this has a limited range and can quickly run up against manufacturing tolerances or material strength requirements. In order to achieve greater or more robust reductions, the screw radius has to be increased, or the driving motor has to have a larger reduction before driving the screw, both of which usually result in more material (typically steel) and therefore more mass.

However, TSA does have some disadvantages, the most significant of which is a nonlinear reduction equation, which is also dependent on the motor angle (and therefore actuator position). The reduction decreases in a nonlinear fashion as the angle increases, with the derivative decreasing as the angle increases. There is also the compliance of the strings to consider, depending on the thickness and material chosen, which becomes a significant factor under high forces. Both of these issues can be addressed with accurate modelling [8] and/or a robust control strategy, as demonstrated in [4]. What is more of an issue is the unidirectional force of the TSA, which can only impart force in tension. This means that for an AUJ, which is a 2 degree of freedom (DOF) joint, a minimum of three TSA are required, unless spring return mechanisms are used, which would impart additional force on the TSA and therefore reduce performance. However, the potential high force ratio of the TSA due to the non-proportional

reduction may adequately compensate for the additional actuator requirement.

The focus of this research is to investigate if the TSA is a suitable candidate for control of an AUJ considering both the benefits and drawbacks. To this end, the objective is to simulate a model and then construct a physical experimental prototype to validate the proposed control system.

The use of TSA as an actuator for an AUJ is an under-studied area of research. **bombara2021physics** have proposed a similar design using a flexible core with continuous curvature as opposed to a rigid universal joint, however currently this research has not demonstrated control of both axes of motion with multiple TSA. For the first time the authors demonstrate a robust closed loop control of an AUJ in both axes of motion using three TSA in an “antagonistic triad” configuration. The result is a light, compact AUJ design that has the potential to significantly improve upon exiting inline actuation options.

This publication will first give an outline of the TSA based on the existing literature, and the concept of an antagonistic triad. Then a detailed explanation of the control system is given, followed by results from the simulation and experimental system. Finally, a theoretical analysis of the TSA AUJ compared to a similar AUJ using leadscrews is conducted, followed by a discussion and conclusion.

This work was previously published as a conference proceeding at the International Conference on Robotics and Automation (ICRA) 2022 [9]. This publication extends that research by...

#### A. A Twisted string actuator

First developed by Würtz, May, Holz, *et al.* [4] in 2010, TSA uses two or more strings between two fixtures as a 1 DOF linear actuator. When one fixture is rotated (typically by an electric motor), the strings twist into a helix, decreasing the distance between the fixtures, as shown in figure 1. Given the unwound length  $l_u$ , and the cross-section radius of the string  $r_s$  (or  $r_s + r_c$  when there are more than two strings) as shown in figure 2, the actuator length is given by

$$l_s(\theta_s) = \sqrt{l_u^2 - \theta_s^2 r_s^2} \quad (1)$$

where  $\theta_s$  is the motor angle, as shown in figure 3.

This equation assumes an infinite string stiffness, so is only reasonably accurate under low tension. Although theoretically the stroke of the TSA can be the entire domain of  $[0, l_u]$ , in reality the thickness of the string prevents a geometric helix from forming once the helix pitch  $q < 4r_s$  (or  $q < 2nr_s$  for  $n$  strings). This limits the lower bound of the stroke as follows,

$$l_{min} = \frac{l_u}{\sqrt{\frac{\pi^2}{2} + 1}} \approx 0.46 l_u \quad (2)$$

or approximately 46% of  $l_u$  for a two string TSA.

$$\theta_s = 0 \quad \theta_s = 2\pi \quad \theta_s = 20\pi$$

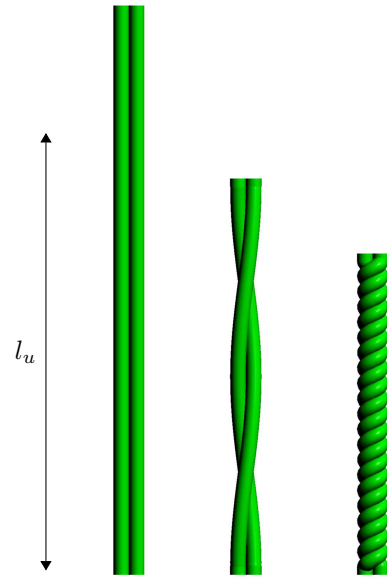


Fig. 1: The value of  $\theta_s$  increases the number of twists in a string bundle with a string length  $l_u$ .

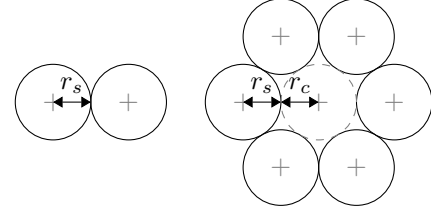


Fig. 2: The location of  $r_s$  and optionally  $r_c$  in a string bundle.

#### B. Antagonistic Triad

As mentioned in the introduction, because the TSA provides only tensile force, a minimum of three actuators are required for a 2 DOF actuation system. These can be arranged in a triangular configuration to create an “antagonistic triad”, akin to the antagonistic pairs of muscles found in animals. Where a revolute joint would be found between the connecting ends of the actuator, a universal joint is found instead. The geometric structure of the system as shown in figure 4 can be described with two equilateral triangles of exradius  $r$  on two planes separated in the  $z$  axis. The centroids are then connected via a universal joint from each plane normal to an intersecting point, let the vector  $\boldsymbol{\theta} = [\theta_1 \ \theta_2]$  denote the rotation of the second plane relative to the first, in the  $x$  and  $y$  axes around the intersecting point, and let  $l_1$  and  $l_2$  denote the normal distance from the intersection to the first and second plane centroids respectively. When  $\boldsymbol{\theta} = [0 \ 0]$  the triangles are parallel to each other. The distance between the vertex pairs of each triangle is then denoted as  $[\lambda_1 \ \lambda_2 \ \lambda_3]$  for the “top”, “left” and “right” vertices of the triangles. When  $\boldsymbol{\theta}$  is changed, this will change  $\lambda_1$ ,

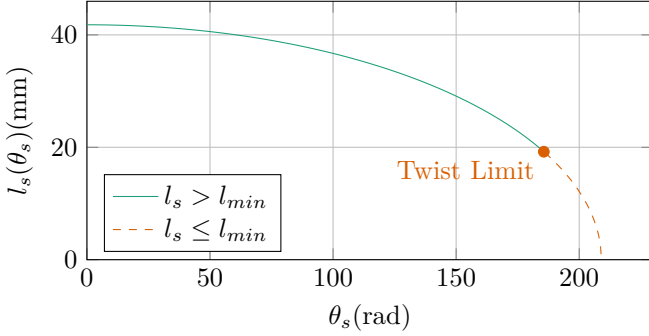


Fig. 3: TSA string length against motor angle with coefficients from table I.

$\lambda_2$  and  $\lambda_3$  respectively.

To calculate the lengths of the strings for a given  $\theta$  of the universal joint, a transformation matrix for each string can be computed, following a path from one vertex to the other via the plane normals. This incorporates the universal joint rotations  $R_1(\theta_1)$  and  $R_2(\theta_2)$ , the normal distance translations  $P_l(l_1)$  and  $P_l(l_2)$ , the triangle exradius translation  $P_r$  and triangle exradius rotation  $R_r(\phi)$ , where  $\phi = [0, \frac{2\pi}{3}, \frac{4\pi}{3}]$  to represent the three vertices of the triangle, hereafter referred to as *top*, *left* and *right*.

$$\begin{aligned} R_1(\theta_1) &= \begin{bmatrix} \cos \theta_1 & 0 & \sin \theta_1 & 0 \\ 0 & 1 & 0 & 0 \\ -\sin \theta_1 & 0 & \cos \theta_1 & 0 \\ 0 & 0 & 0 & 1 \end{bmatrix} \\ R_2(\theta_2) &= \begin{bmatrix} 0 & 0 & 0 & 1 \\ 0 & \cos \theta_2 & -\sin \theta_2 & 0 \\ 0 & \sin \theta_2 & \cos \theta_2 & 0 \\ 0 & 0 & 0 & 1 \end{bmatrix} \\ P_l(l) &= \begin{bmatrix} 1 & 0 & 0 & 0 \\ 0 & 1 & 0 & 0 \\ 0 & 0 & 1 & l \\ 0 & 0 & 0 & 1 \end{bmatrix} \\ P_r &= \begin{bmatrix} 1 & 0 & 0 & 0 \\ 0 & 1 & 0 & r \\ 0 & 0 & 1 & 0 \\ 0 & 0 & 0 & 1 \end{bmatrix} \\ R_r(\phi) &= \begin{bmatrix} \cos \phi & -\sin \phi & 0 & 0 \\ \sin \phi & \cos \phi & 0 & 0 \\ 0 & 0 & 1 & 0 \\ 0 & 0 & 0 & 1 \end{bmatrix} \end{aligned} \quad (3)$$

$$T_n(\theta) = P_l(l_1) R_1(\theta_1) R_2(\theta_2) P_l(l_2)$$

$$T_1(\theta) = P_r^{-1} T_n(\theta) P_r$$

$$T_2(\theta) = R_r\left(\frac{2\pi}{3}\right) P_r^{-1} R_r\left(-\frac{2\pi}{3}\right) T_n(\theta) R_r\left(\frac{2\pi}{3}\right) P_r$$

$$T_3(\theta) = R_r\left(-\frac{2\pi}{3}\right) P_r^{-1} R_r\left(\frac{2\pi}{3}\right) T_n(\theta) R_r\left(-\frac{2\pi}{3}\right) P_r$$

Then, to get the distances between the vertex pairs, the euclidean norm for the position components of each transformation matrix  $T$  can be calculated. These distances can then be combined into a vector function  $\Lambda(\theta) = [\lambda_1(\theta) \ \lambda_2(\theta) \ \lambda_3(\theta)]$ .

$$\begin{aligned} \ell(T) &= \| [t_{14} \ t_{24} \ t_{34}] \|_2 \\ \Lambda(\theta) &= [\ell(T_1(\theta)) \ \ell(T_2(\theta)) \ \ell(T_3(\theta))] \\ &= [\lambda_1(\theta) \ \lambda_2(\theta) \ \lambda_3(\theta)] \end{aligned}$$

where:

$$\lambda_1(\theta) = \sqrt{l_1^2 + 2l_1l_2 \cos(\theta_1) \cos(\theta_2) + 2l_1r \sin(\theta_1) \cos(\theta_2) + l_2^2 + 2l_2r \sin(\theta_2) - 2r^2 \cos(\theta_2) + 2r^2}$$

$$\lambda_2(\theta) = \sqrt{a + b + c - d}$$

$$\lambda_3(\theta) = \sqrt{a - b - c + d}$$

where:

$$\begin{aligned} a &= l_1^2 + 2l_1l_2 \cos(\theta_1) \cos(\theta_2) \\ b &= \sqrt{3}l_1r \sin(\theta_1) - l_1r \sin(\theta_2) \cos(\theta_1) + l_2^2 \\ c &= \sqrt{3}l_2r \sin(\theta_1) \cos(\theta_2) - l_2r \sin(\theta_2) \\ d &= \frac{\sqrt{3}r^2 \sin(\theta_1) \sin(\theta_2)}{2} - \frac{3r^2 \cos(\theta_1)}{2} - \frac{r^2 \cos(\theta_2)}{2} + 2r^2 \end{aligned} \quad (4)$$

The output of this is shown in figure 5 for a domain of  $[-\frac{\pi}{2}, \frac{\pi}{2}]$ .

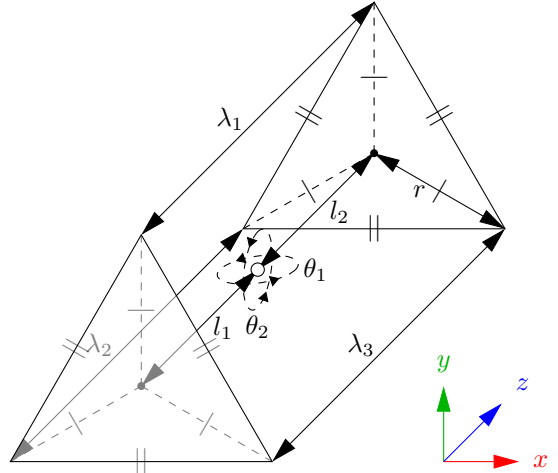


Fig. 4: Kinematic diagram of the antagonistic triad, where the universal joint rotation is defined by  $\theta_{1,2}$  on the *y* and *x* axes respectively, and the actuator lengths are defined by  $\lambda_{1,2,3}$  for the *top*, *left* and *right* strings.  $r$  and  $l_{1,2}$  define the anchor points of the strings.

## II. CONTROL SYSTEM

The control system is a four layer cascade design, joining an inverse dynamic control system [10], to the triad force controller in [11], to a proportional controller for each TSA. It uses feedback signals of the joint position from the accelerometers and TSA force from the load cells. A second order setpoint trajectory  $q$  is used as the input, which can either be pre-defined or generated dynamically from user input. Feedback is provided by the AUJ angular position  $\theta$  as shown in figure 4, angular velocity  $\dot{\theta}$ , and TSA tension force  $\hat{f}$ . Figure 7 shows a complete block diagram of the control system.



Fig. 5: Surface plots of each element of the vector function  $\Lambda(\theta)$ , assuming coefficient values from table I. Note that  $\lambda_2$  and  $\lambda_3$  are symmetric.

- 1)  $C_1$  AUJ Position PID Controller
- 2)  $C_2$  Inverse Dynamics
- 3)  $C_3$  TSA Force Optimisation Algorithm
- 4)  $C_4$  TSA Force P Controller

Functions  $C_{1\dots 4}$  are then combined into a cascade function  $C_4(C_3(C_2(C_1(\dots),\dots),\dots),\dots)$ .

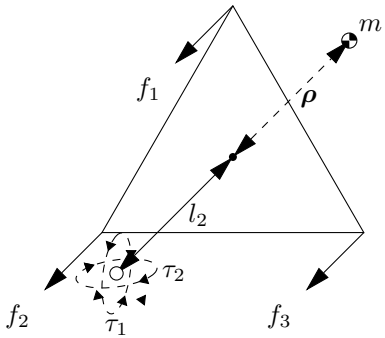


Fig. 6: Dynamics of an antagonistic triad based on figure 4, where the follower mass is  $m$ , the follower center of mass (COM) relative to the universal joint pivot is  $\rho$ , the forces on each anchor point are  $f_{1,2,3}$  and the universal joint torque is  $\tau_{1,2}$ .

#### A. Actuated universal joint Position PID Controller with Acceleration Feedforward

Firstly, a PID controller is used to generate a control signal  $\mathbf{u}$  with the input  $\mathbf{q}$  as the setpoint, and the AUJ angular position  $\theta$  and velocity  $\dot{\theta}$  as feedback, plus the addition of a feedforward term for the input acceleration  $\ddot{\mathbf{q}}$ , i.e.

$$\mathbf{u} = \mathbf{k}_p(\mathbf{q} - \theta) + \mathbf{k}_i \left( \int_0^t (\mathbf{q} - \theta) dt \right) + \mathbf{k}_d (\dot{\mathbf{q}} - \dot{\theta}) + \ddot{\mathbf{q}}. \quad (5)$$

In the discrete implementation used for fixed step simulation and experimental system control, the integral term is replaced by the trapezoidal rule.

$$K_I \int_0^t \epsilon \approx \sum_{i=0}^N \frac{\epsilon(t_i) + \epsilon(t_{i-1})}{2} \Delta t \quad (6)$$

#### B. Inverse Dynamics

The control signal  $\mathbf{u}$  from the PID controller is then converted to the desired AUJ torque  $\boldsymbol{\tau}$ . Firstly the affine transformation matrix  $T(\theta)$  for a coordinate frame between the AUJ pivot and the COM of the follower segment can be defined, with the rotation matrices  $R_1(\theta_1)$  and  $R_2(\theta_2)$  defining the orientation of the universal joint, and  $P$  defining the offset between the center of the universal joint and the follower mass. The order of  $R_1(\theta_1)$  and  $R_2(\theta_2)$  can be reversed, but this requires other terms to be reversed as well.

$$P = \begin{bmatrix} 1 & 0 & 0 & \rho_1 \\ 0 & 1 & 0 & \rho_2 \\ 0 & 0 & 1 & l_2 + \rho_3 \\ 0 & 0 & 0 & 1 \end{bmatrix} \quad (7)$$

$$T(\theta) = R_1(\theta_1) R_2(\theta_2) P$$

Then the linear velocity jacobian  $J_v$  is simply the jacobian of the translation vector of  $T$ .

$$J_v(\theta) = \begin{bmatrix} \frac{\partial t_{14}}{\partial \theta_1} & \frac{\partial t_{24}}{\partial \theta_1} & \frac{\partial t_{34}}{\partial \theta_1} \\ \frac{\partial t_{14}}{\partial \theta_2} & \frac{\partial t_{24}}{\partial \theta_2} & \frac{\partial t_{34}}{\partial \theta_2} \end{bmatrix} \quad (8)$$

The angular velocity jacobian  $J_\omega$  is calculated using the first joint angle relative to the base frame, and the second in the frame of the first. If  $R_x$  is the first rotation in  $T$  then the first column of the jacobian is  $[100]^\top$  (to represent the pitch angle) and the second column is  $R_x [010]^\top$ .

$$J_\omega(\theta) = \begin{bmatrix} 1 & r_{x_{11}} \\ 0 & r_{x_{21}} \\ 0 & r_{x_{31}} \end{bmatrix} \quad (9)$$

Then the mass matrix  $D$  can be created from the jacobian, the mass for the follower segment  $m$  and its inertia tensor  $I \in \mathbb{R}^{3 \times 3}$ , and  $R_x$  and  $R_y$  to express the inertia in the correct frame.

$$D(\theta) = m J_v^\top J_v + J_\omega^\top (R_x R_y) I (R_x R_y)^\top J_\omega^\top \quad (10)$$

The centrifugal/coriolis matrix  $C$  is created from the christoffel symbols of  $D$ , along with the AUJ velocity vector  $\dot{\theta}$ .



Fig. 7: Block diagram of the complete experimental control system, excluding the hardware velocity controllers for the motors.

$$C(\theta, \dot{\theta})_{k,j} = \sum_{i=1}^N \frac{1}{2} \frac{\partial d_{kj}}{\partial \theta_i} + \frac{\partial d_{ki}}{\partial \theta_j} - \frac{\partial d_{ij}}{\partial \theta_k} \dot{\theta}_i \quad (11)$$

Then the gravity term  $G$ . As the gravity vector direction is the same as the z axis as in figure 4, the height is equal to  $-l_2 \cos \theta_1 \cos \theta_2$ , therefore the potential energy is  $mg(-l_2 \cos \theta_1 \cos \theta_2)$ . The jacobian of this then becomes the gravity term.

$$G(\theta) = \begin{bmatrix} \frac{\partial mg - l_2 \cos \theta_1 \cos \theta_2}{\partial \theta_1} \\ \frac{\partial mg - l_2 \cos \theta_1 \cos \theta_2}{\partial \theta_2} \end{bmatrix} \quad (12)$$

$D$ ,  $C$  and  $G$  are then combined to form the dynamics equation  $C_2$ , along with the AUJ position and velocity vectors.  $C_1$  is used as the acceleration term. This results in a setpoint joint torque which can be used in the optimisation algorithm.

$$\tau = D(\theta)u + C(\theta, \dot{\theta})\dot{\theta} + G(\theta). \quad (13)$$

### C. Twisted string actuator Force Optimisation Algorithm

This uses the *inverse force transformation* algorithm from [11] with the jacobian of equation 4 to select an optimal force vector from the desired joint torque. Here it is presented in an unexpanded and more general form. A force matrix  $F$  is created from the torque input  $\tau$ , jacobian  $J_\Lambda$  from the vector function  $\Lambda$  as defined in equation 4, and minimum force constant  $f_{min}$ .  $f_{ii}$  is equal to  $f_{min}$ , while the other elements in the column are based on a calculation using  $J_{\Lambda_{-i,*}}$  where  $-i$  is a row removed from the matrix.

$$\begin{aligned} J_\Lambda &= \begin{bmatrix} \frac{\partial \lambda_1}{\partial \theta_1} & \frac{\partial \lambda_2}{\partial \theta_1} & \frac{\partial \lambda_3}{\partial \theta_1} \\ \frac{\partial \lambda_1}{\partial \theta_2} & \frac{\partial \lambda_2}{\partial \theta_2} & \frac{\partial \lambda_3}{\partial \theta_2} \end{bmatrix} \\ \gamma(i) &= -J_{\Lambda_{-i,*}}^{-T} (J_{\Lambda_{i,*}}^T f_{min} + \tau) \quad (14) \\ F(\tau, \theta) &= \begin{bmatrix} f_{min} & \gamma(2)_1 & \gamma(3)_1 \\ \gamma(1)_1 & f_{min} & \gamma(3)_2 \\ \gamma(1)_2 & \gamma(2)_2 & f_{min} \end{bmatrix} \end{aligned}$$

The following algorithm then selects one column of  $F$  to be the output force vector  $f$ , where  $\top$  and  $\perp$  are boolean *true* and *false* respectively, and  $f_{*,i}$  is the  $i$ th column of  $F$ . The solution to this algorithm minimises the net force on all TSA while producing the desired output torque on the universal joint.

```

1:  $s \leftarrow [\top \top \top]$ 
2: if  $f_{23} > f_{min}$  then  $s_2 \leftarrow \perp$  else  $s_3 \leftarrow \perp$  end if
3: if  $f_{31} > f_{min}$  then  $s_3 \leftarrow \perp$  else  $s_1 \leftarrow \perp$  end if
4: if  $f_{12} \geq f_{min}$  then  $s_1 \leftarrow \perp$  else  $s_2 \leftarrow \perp$  end if
5: for  $i = 1$  to  $3$  do
6:   if  $s_i \rightarrow \top$  then  $f \leftarrow f_{*,i}$  end if
7: end for

```

### D. Twisted string actuator Force Proportional Controller

The selected forces are then used as an input to a P controller with gain  $k_{p_s}$  using the measured load cell forces  $\hat{f}$  as feedback. The output from this can then be used to control the top, left and right TSA motors, corresponding to the actuators in figure 4.

1) *Simulation Current Control*: In the simulation, each TSA was modelled as a state-space system which takes motor current  $u$  as an input and outputs  $y$  as the TSA tension force. [4] defines it as such, where  $J$  is the motor inertia,  $C$  is the motor coulomb friction (modified from viscous friction as the motor only has dry friction),  $K_t$  is the motor torque constant, and  $K_L$  is the load stiffness. As the original definition is for a fixed load  $l_u$  distance from the motor a modified model is required which takes into account the varying length between the motor and load defined by  $\Lambda(\theta)$ . A saturation function, with the compact notation  $\text{sat}_x^y z = \max(x, \min(y, z))$  is used to prevent incorrect compression forces when the string is slack. All of the motor coefficients were taken from the Faulhaber 1724TSR datasheet [12] as this is the motor used in the experimental model. An estimated value is used for the load stiffness, this was chosen to be a high number as the model is expected to be very stiff.

$$\begin{aligned}
h(\theta_s) &= \frac{\theta r_s^2}{\sqrt{l_u^2 - \theta_s^2 r_s^2}} \\
k(\theta_s, \boldsymbol{\theta}) &= \lambda_n(\boldsymbol{\theta}) - \sqrt{l_u^2 - \theta_s^2 r_s^2} \\
\dot{\boldsymbol{x}} &= \begin{bmatrix} x_2 \\ -\frac{K_L}{J} h(x_1) k(x_1, \boldsymbol{\theta}) - \frac{C}{J} \operatorname{sgn}(x_2) \end{bmatrix} + \begin{bmatrix} 0 \\ \frac{K_t}{J} \end{bmatrix} u \\
y &= K_L \operatorname{sat}_0^\infty k(x_1, \boldsymbol{\theta})
\end{aligned} \tag{15}$$

The state space model was then adapted to include constraints on motor velocity and acceleration set by the motor controller in order to keep the motor within design limits, by replacing  $\dot{\boldsymbol{x}}$  with  $\dot{\boldsymbol{x}}'$  which contains saturation functions for maximum motor velocity  $v_s$  and acceleration  $\alpha_s$ .

$$\dot{\boldsymbol{x}}' = \begin{bmatrix} \operatorname{sat}_{-\omega_s}^{\omega_s} \dot{x}_1 \\ \operatorname{sat}_{-\alpha_s}^{\alpha_s} \dot{x}_2 \end{bmatrix} \tag{16}$$

*2) Experimental Velocity Control with Deadband Compensation:* Due to a controller deadband within  $\pm 10 \text{ min}^{-1}$ , an adjustable deadband compensator is used,

$$\phi_i(\omega_i) = \begin{cases} 10 & 10 \leq \omega_i < h \\ -10 & -h < \omega_i \leq -10 \\ 0 & h \leq \omega_i \leq -h \\ \omega_i & \text{otherwise} \end{cases} \tag{17}$$

where  $\phi_i$  is the compensator for the controller  $i$ . An adjustment value  $h \in [0, 10]$  changes the threshold at which the compensator switches on and off, allowing for a small deadband to remain.

The result from the TSA is then a compressive force acting between each of the three TSA and its corresponding endpoint on the Antagonistic Triad, imparting a torque on the axes of the universal joint.

### III. SIMULATION & EXPERIMENTAL RESULTS

To design and refine the parameters of the control system, a Simscape Multibody™ model of the antagonistic triad and control system was created in MATLAB®/Simulink™. This allowed for model design coefficients  $l_1, 2$  and controller gains  $k_p, k_i, k_d, k_{ps}$  to be modified in order to have the most stable control within design limits.

#### A. Experimental Setup

For the experimental validation, a physical prototype of the mechanism was constructed with coefficients from table I as design parameters. This was mounted vertically, in order for the inertial measurement unit (IMU) to measure the orientation of the universal joint. The TSA mechanisms consist of a compact high torque motor attached to the base segment, with a string clamp attached to the motor shaft. On the follower segment, a load cell is mounted on top of a universal joint to ensure a purely axial load, with a capstan bolt attached to the load cell. The string itself is attached to the clamp at both ends using

TABLE I: Model coefficients.

Coefficient	Value	Coefficient	Value
$l_1$	41.8 mm	$J$	$1 \times 10^{-6} \text{ kg m}^{-2}$
$l_2$	0 mm	$K_L$	$1000 \text{ N m}^{-1}$
$r$	13 mm	$f_{min}$	3 N
$l_u$	41.8 mm	$\omega_s$	$441.9 \text{ rad s}^{-1}$
$r_s$	200 $\mu\text{m}$	$I_s$	0.19 A
$m$	72.619 13 g	$K_t$	$0.0263 \text{ N m A}^{-1}$
$C$	0.1315 N mm	$\tau_s$	4.5 mN m
$\alpha_s$	$1 \times 10^5 \text{ rad s}^{-2}$	$\rho$	[0 0 0] mm
Coefficient	Value		
$I$	$\begin{bmatrix} 3 \times 10^{-5} & 0 & 0 \\ 0 & 3.2 \times 10^{-5} & 0 \\ 0 & 0 & 1.4 \times 10^{-5} \end{bmatrix} \text{ kg m}^{-2}$		

TABLE II: PID gains in the simulation and experiment.

Gain	Value	
	Simulation	Experiment*
$k_p$	800	$3 \times 10^4$
$k_i$	3000	350
$k_d$	50	50
$k_{ps}$	19	100

\* Tracking mode, see section III-B.

two grub screws for extra security and easy adjustment, and looped through the hole in the capstan bolt. The total mass of the prototype, excluding the mount, is  $\approx 176 \text{ g}$ . Figures 8 and 18 detail the construction of the experiment with all the constituent parts.

The motors were controlled by Fauhaber MCDC3002 motor controllers, which could interface with a National Instruments MyRIO via the USB port, using a USB to serial converter. The load cells were Futek LCM100 miniature load cells, selected for their small size. The signals from these were amplified using Flyde FE-359-TA instrumentation amplifiers and decoded using an external AD7606 ADC before being fed into the MyRIO using SPI. The orientation of the AUJ was measured using a Bosch Sensortec BNO080 IMU using the accelerometer data.

#### B. Windup & Tracking States

When the mechanism is started with the TSA in a completely unwound state, before it can begin tracking a motion trajectory, the TSA strings must “wind up” to closely match the initial state of  $\boldsymbol{f}$ . During this phase, the outer PID gains  $k_p, k_i$  are unsuitable and can result in damage to the mechanism. To mitigate this, two sets of PID gains are chosen, one for the windup state ( $k_p = 800$ ,  $k_i = 3000$ ), and another for the tracking state ( $k_p = 3 \times 10^4$ ,  $k_i = 350$ ), which the windup state transitions to once suitable stability is achieved. This transition trigger is defined on a per-axis basis, as the first zero crossing of the angle error (as  $\boldsymbol{q} = 0$  this is effectively  $\boldsymbol{\theta}$ ). A graph showing the difference this state change makes to the AUJ orientation is shown in figure 10.

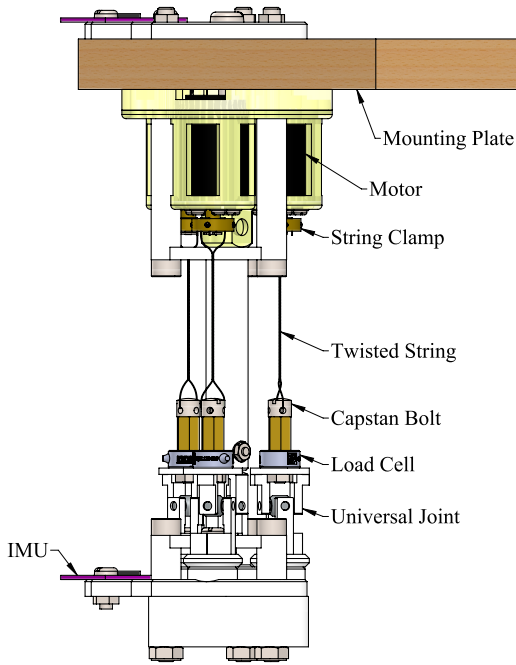


Fig. 8: Schematic of the experimental system with labelled components.

### C. Results

1) *Force Proportional Controller & Motor Characterisation:* Before verifying robust control of the AUJ, the control of each individual TSA needed to be tested in order to characterise the performance of the motors and to ensure the inner loop control system was robust. This would involve selecting the control strategy that gave the best performance. A test trajectory consisting of a smooth ramp followed by a sine wave was fed into the inner loop of the cascade function as  $[f(t) \ f(t) \ f(t)]$ . Each control strategy was tested, and in the end the velocity control strategy proved most optimal, as is shown in figure 11. The results of a sinusoidal force trajectory for the velocity control strategy is shown in figure 12. As can be seen in the inset, there is a stick-slip friction effect which causes a sawtooth like effect on the measured force. This means the motor angle has to be constantly adjusted even with a constant force input, in order to maintain the setpoint force.

2) *Actuated universal joint Angle Tracking:* Figure 13 plots the tracking response of both the simulation and experiment. Three trajectories were created to test the capabilities of the mechanism. Two were only in one axis of the Universal Joint, and the third was in both axes.

### D. The Effect of $f_{\min}$ on AUJ Roll Range Limits

As the TSA use a closed loop force controller, the pitch and roll angle range is determined by the “opposing” TSA motor angle at  $f_{\min}$  when  $\theta = [0 \ 0]$ . This is because

Experiments were able to achieve modest increases of  $\approx 4.004^\circ N^{-1}$  for the positive (upper) limit of the universal joint roll  $\theta_1$ , and  $\approx -6.062^\circ N^{-1}$  for the negative

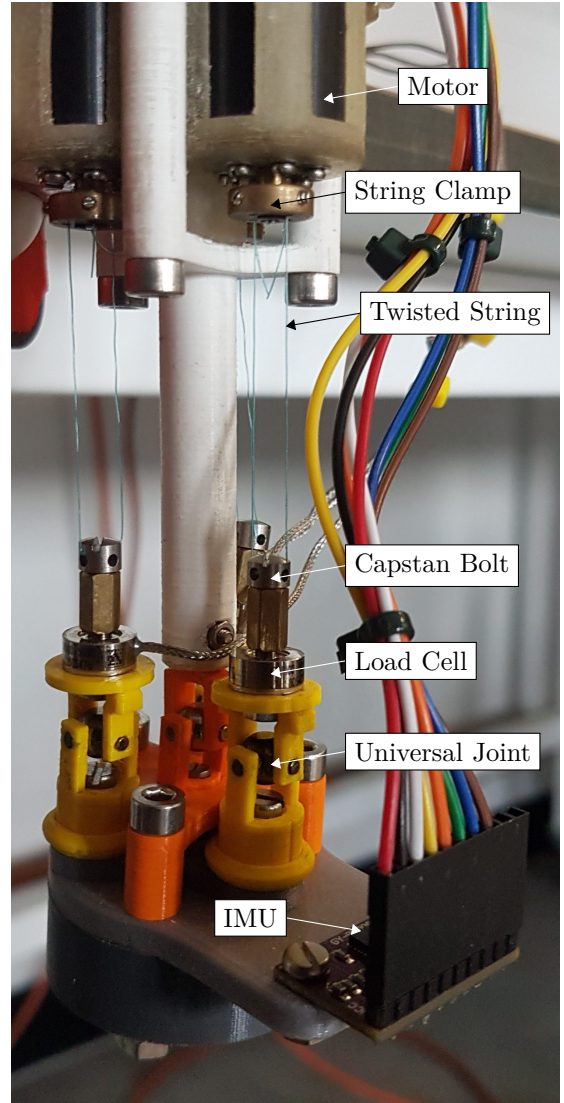


Fig. 9: Annotated photograph of the experimental system.

(lower) limit, within the  $f_{\min}$  interval [3, 3.5], as shown in figure ???. Attempts to increase the upper bound of this interval resulted in the opposing TSA exceeding torsion limits, causing string failure.

### E. The Effect of AUJ Angular Velocity on AUJ Angle Tracking

To verify the performance of the AUJ at higher angular velocities, the single axis experiments from section III-C2 were repeated with a trapezoidal “chirp” signal, with the maximum angular velocity increasing by  $\omega_0 + (2(n-1)\omega_0)$  each cycle, where  $n$  is the cycle number, and  $\omega_0$  is the initial maximum angular velocity, and the angular acceleration increasing by  $\alpha_0 + (16(n-1)\alpha_0)$  each cycle, where  $\alpha_0$  is the initial angular acceleration. A total of four cycles were performed, with the maximum velocity and acceleration values shown in table III. Figure 15 shows the results of these experiments, which shows the tracking error increasing marginally as maximum angular velocity and acceleration increases.

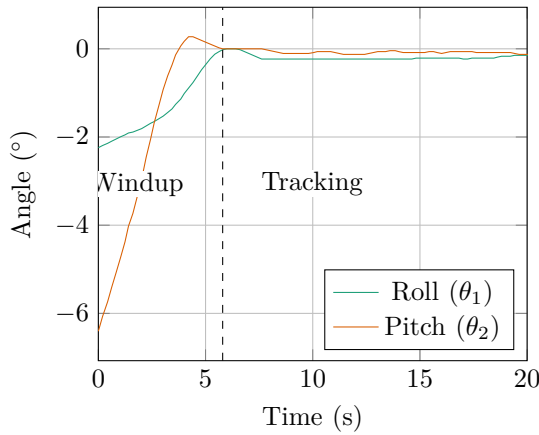


Fig. 10: The initial startup of the mechanism showing the transition between “windup” and “tracking” states.

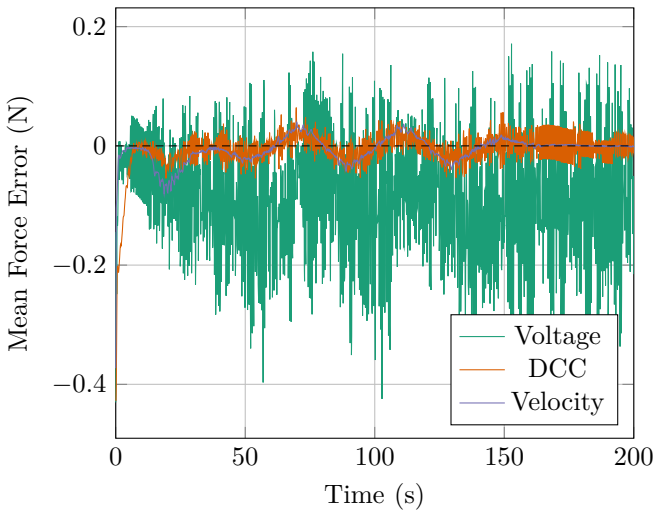


Fig. 11: Mean tracking error for each control strategy.

#### F. The Effect of Follower Mass on AUJ Angle Tracking

In order to demonstrate the feasibility of a multiple joint system, additional mass was added to the follower segment and the *Pitch & Roll* trajectory was performed to analyze the effect of the additional mass on the control system. This was performed by the modification of the end of the follower segment to allow multiple standard disc weights, each with a mass of 100 g, to be attached. Four experiments were performed, one with no disc weights attached, and three with one, two, and three disc weights attached, adding approximately 100 g each time. 3D printed custom length spacers were used to maintain an approximately

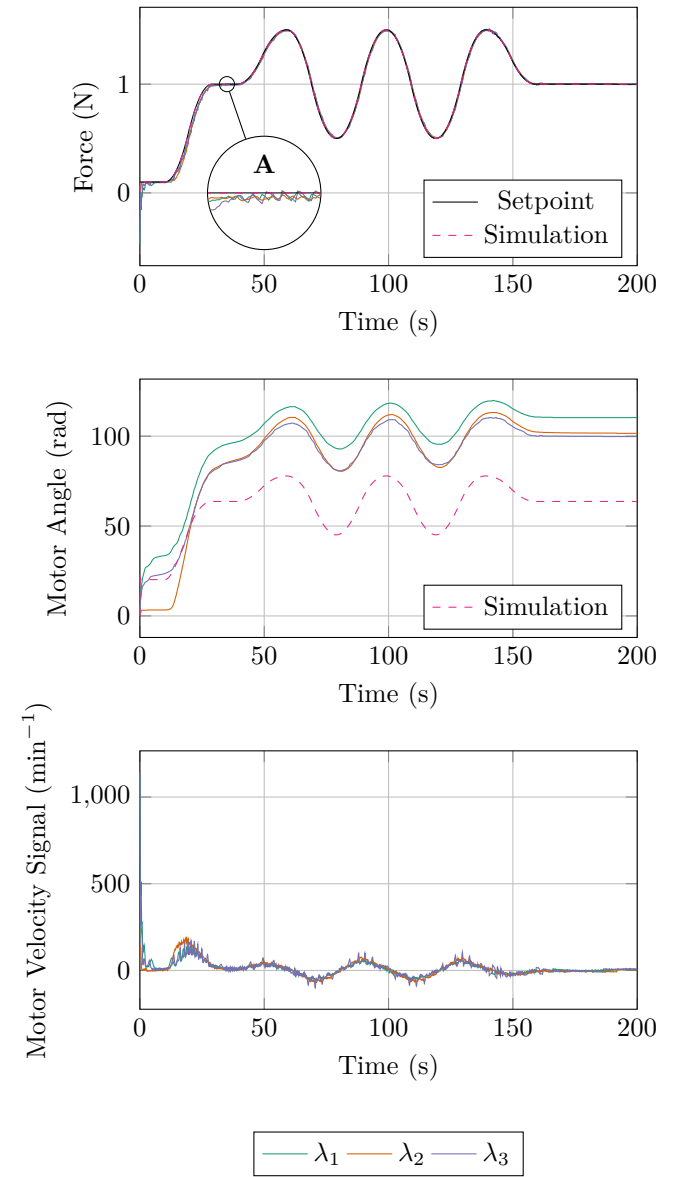


Fig. 12: Load cell, motor angle, and motor velocity signal plot from each string using the velocity control strategy for an experimental trajectory. Inset A shows a zoomed in portion of the graph, illustrating the stick-slip phenomenon noticed in the load cell measurements.

equal COM for each of the experiments with disc weights. Figure ?? shows each configuration of the follower segment for the experiments. Table IV lists the four follower mass configurations that were tested, with follower mass and inertia matrix  $m$  and  $I$ , and follower COM z component  $\rho_3$ . The follower COM x and y components were set to 0 for these experiments, as they did not vary significantly between experiments, and had a negligible contribution to the dynamics. These figures are based on estimates from a computer aided design (CAD) model developed in SolidWorks®, with known weights of 100 g. Any inertial terms less than  $1 \times 10^{-5}$  were rounded down to 0, which resulted in a diagonal inertia matrix. For each experiment,

Cycle	Max./Min. Angle [rad]	Max. Velocity [rad s⁻¹]	Acceleration [rad s⁻²]
1	0.2	0.01	0.00125
2	0.2	0.03	0.02125
3	0.2	0.05	0.04125
4	0.2	0.07	0.06125

TABLE III

the inverse dynamics parameters  $m$  and  $\rho$  were updated so the correct setpoint torque would be calculated.

Figure 16 shows the setpoint and response trajectory for each experiment. Initially,  $k_p$  was set to the same value as in table I, however the system was unable to reach a steady state in any configuration other than “No Mass”. Reducing  $k_p$  to 1000 in the weighted configurations solved the steady state issue and resulted in an average maximum tracking error of  $0^\circ$  over all configurations with added mass, similar to the result from the initial experiments. However, for the “No Mass” configuration,  $k_p = 1000$  resulted in a very poor tracking response, whereas  $k_p$  from table I resulted in a maximum tracking error of  $0^\circ$ , once again similar to the result from the initial experiments. In future implementations gain scheduling can be employed to select the most optimal  $k_p$  for a given follower mass, that allows for the smallest tracking error while being able to reach a steady state.

#### IV. PERFORMANCE

##### A. TSA Comparison with Leadscrew

To compare the performance of a TSA AUJ against alternatives, we can measure two metrics, the maximum tension force  $f_{max}$  and maximum stroke velocity  $\dot{p}_{max}$ . This corresponds to the equivalent of maximum torque and maximum velocity in a rotary motor, a larger  $f_{max}$  would be able to actuate a larger follower mass, and a larger  $\dot{p}_{max}$  would be able to rotate the AUJ more quickly. The alternatives chosen for comparison are leadscrews of various rod diameters  $d_m$  and pitches  $\lambda$ , and a “direct drive” where the motor is rotating the universal joint directly without any reduction or motion transformation.

1) *Twisted string actuator*: For the TSA metrics, the equations from [4], in particular  $h(\theta)$  and  $k(\theta)$  as used for the state space, which can be used to determine  $f_{max}$  and  $\dot{p}_{max}$ . By extracting coefficient  $r_s$  as an input to make  $f(p, r_s)$  and  $\dot{p}(\dot{\theta}, p, r_s)$  the performance of different string thicknesses can be compared for a given unwound length  $l_u$  and  $\tau_{k(\theta)} = l_u - \sqrt{l_u^2 - \theta_s^2 r_s^2}$

$$\begin{aligned} k^{-1}(p) &= \pm \frac{\sqrt{p(2l_u - p)}}{r_s} \\ h^{-1}(\theta) &= \frac{\sqrt{l_n^2 - r_s^2 \theta^2}}{r_s^2 \theta} \end{aligned} \quad (18)$$

$$f(p) = h^{-1}(k^{-1}(p)) = \pm \frac{\sqrt{(l_u - p)^2}}{r_s \sqrt{p(2l_u - p)}}$$

$$f_{max} = f(p)\tau_{max}$$

$$\begin{aligned} k(\dot{\theta}, \theta) &= \frac{\dot{\theta} r_s^2 \theta}{\sqrt{l_n^2 - r_s^2 \theta^2}} \\ \dot{p}(\dot{\theta}, p) &= k(\dot{\theta}, k^{-1}(p)) = \pm \frac{\dot{\theta} r_s \sqrt{p(2l_n - p)}}{\sqrt{(l_n - p)^2}} \\ \dot{p}_{max} &= \dot{p}(\dot{\theta}_{max}, p) \end{aligned} \quad (19)$$

2) *Leadscrew*: For the leadscrew metrics, the raising torque calculation [13] can be used as the absolute value of  $f_{max}$ , since the TSA only operates in tension, which can be used to determine the same metrics. The performance of different screw diameters  $d_m$  and leads  $\lambda$  can then be compared for a given  $\tau_{max}$  and coefficient of friction  $\mu$ .  $\dot{p}_{max}$  is then calculated by multiplying  $\lambda$  with  $\dot{\theta}_{max}$ . The performance of different  $\lambda$  can then be compared for a given  $\dot{\theta}_{max}$ .

$$\begin{aligned} |\tau(f)| &= \frac{d_m f(\lambda + \pi d_m \mu)}{2(\pi d_m - \lambda \mu)} \\ |f(\tau)| &= \frac{2\tau(\pi d_m - \lambda \mu)}{d_m(\lambda + \pi d_m \mu)} \\ f_{max} &= |f(\tau_{max})| \end{aligned} \quad (20)$$

$$\begin{aligned} \dot{p}(\dot{\theta}) &= \lambda \frac{\dot{\theta}}{2\pi} \\ \dot{p}_{max} &= \dot{p}(\dot{\theta}_{max}) \end{aligned} \quad (21)$$

3) *Direct Drive*: The direct drive metrics are trivially calculated using the lever force and tangential velocity that would be generated at the endpoint of a linear actuator able to impart equivalent angular velocity and torque on the universal joint.

$$f_{max} = \frac{\tau_{max}}{\sqrt{l_2^2 + r^2}} \quad (22)$$

$$\dot{p}_{max} = \dot{\theta}_{max} \sqrt{l_2^2 + r^2} \quad (23)$$

4) *Comparison between TSA and Leadscrew*: As the values for  $\tau_{max}$  and  $\dot{\theta}_{max}$  for the TSA depend on  $p$ , but remain constant for the leadscrew, the performance of the TSA is going to be better or worse than a given leadscrew depending on the value  $p$ . Figure 17 compares the TSA configuration using the coefficients from table I against a number of common leadscrew configurations that are practical for the dimensions of the AUJ. The TSA outperforms or underperforms different leadscrew configurations depending on  $p$ . In simpler terms, the performance of the TSA is dependent on the contraction length. The maximum linear velocity increases with the contraction length, and the maximum tension force decreases with contraction length, both in a nonlinear fashion.

##### B. String Material Selection

#### V. DISCUSSION & CONCLUSION

##### A. Discussion

Upon reflection of the research conducted and the results obtained, future developments would include improvements to the orientation sensors, the data from the IMU proved to be unreliable and of poor resolution ( $2.0^\circ$  static,  $3.5^\circ$  dynamic). The magnetometer was unusable within the indoor experimental environment even after several calibration attempts, so the universal joint angle would not be able to be calculated when the gravity vector

Configuration	$m$ [g]	$\rho_3$ [mm]	$I$ [kg m <sup>-2</sup> ]
No Mass	67	6.7	$\begin{bmatrix} 3.3 \times 10^{-5} & 0 & 0 \\ 0 & 3.1 \times 10^{-5} & 0 \\ 0 & 0 & 1.4 \times 10^{-5} \end{bmatrix}$
+100 g	170	49	$\begin{bmatrix} 1.3 \times 10^{-4} & 0 & 0 \\ 0 & 1.3 \times 10^{-4} & 0 \\ 0 & 0 & 4.6 \times 10^{-5} \end{bmatrix}$
+200 g	220	50	$\begin{bmatrix} 1.7 \times 10^{-4} & 0 & 0 \\ 0 & 1.7 \times 10^{-4} & 0 \\ 0 & 0 & 7.7 \times 10^{-5} \end{bmatrix}$
+300 g	320	50	$\begin{bmatrix} 2.0 \times 10^{-4} & 0 & 0 \\ 0 & 2.0 \times 10^{-4} & 0 \\ 0 & 0 & 1.1 \times 10^{-4} \end{bmatrix}$

TABLE IV: Table of all the follower mass configurations, with the parameters for follower mass  $m$  and follower COM z offset  $\rho_3$ .

is not orthogonal to the universal joint DOF. An alternative method for sensing the universal joint orientation should be investigated, such as linear variable differential transformers (LVDTs), hall effect sensors or potentiometers. Alternative control algorithms that are less or not dependant on the dynamic properties of the follower segments (mass and inertia) will also be considered, in order to improve the robustness of the control system to external forces. The 1724TSR motors also had poor performance at low speeds, necessitating the deadband compensator. Investigating the use of similar size and torque brushless motors with sinusoidal commutation for stable low speed control could eliminate the need for the compensator, and allow for smoother AUJ motion. Development of a system comprised of multiple segments is the eventual goal, to demonstrate its suitability for applications such as mobile snake robots or snake-arm robots. This can use a embedded controller for each segment, controlled by a master controller for individual joint control or inverse kinematics, as in figure ??.

## B. Conclusion

### REFERENCES

- [1] R. Buckingham and A. Graham, “Nuclear snake-arm robots,” *Industrial Robot: An International Journal*, 2012.
- [2] M. Luo, R. Yan, Z. Wan, et al., “Orisnake: Design, fabrication, and experimental analysis of a 3-d origami snake robot,” *IEEE Robotics and Automation Letters*, vol. 3, no. 3, pp. 1993–1999, 2018.
- [3] W. S. Rone, W. Saab, and P. Ben-Tzvi, “Design, Modeling, and Integration of a Flexible Universal Spatial Robotic Tail,” *Journal of Mechanisms and Robotics*, vol. 10, no. 4, Apr. 2018, 041001, ISSN: 1942-4302. doi: 10.1115/1.4039500.
- [4] T. Würtz, C. May, B. Holz, C. Natale, G. Palli, and C. Melchiorri, “The twisted string actuation system: Modeling and control,” in *2010 IEEE/ASME International Conference on Advanced Intelligent Mechatronics*, 2010, pp. 1215–1220. doi: 10.1109/ AIM.2010.5695720.
- [5] P. Muehlbauer, M. Schimbera, K. Stewart, and P. P. Pott, “Twisted string actuation for an active modular hand orthosis,” in *ACTUATOR; International Conference and Exhibition on New Actuator Systems and Applications 2021*, VDE, 2021, pp. 1–4.
- [6] J. Park, J.-i. Park, H.-T. Seo, Y. Liu, K.-S. Kim, and S. Kim, “Control of tendon-driven (twisted-string actuator) robotic joint with adaptive variable-radius pulley,” in *2020 20th International Conference on Control, Automation and Systems (ICCAS)*, IEEE, 2020, pp. 1096–1098.
- [7] B. Suthar and S. Jung, “Design and feasibility analysis of a foldable robot arm for drones using a twisted string actuator: Frad-tsa,” *IEEE Robotics and Automation Letters*, vol. 6, no. 3, pp. 5769–5775, 2021. doi: 10.1109/LRA.2021.3084890.
- [8] S. Nedelchev, I. Gaponov, and J. Ryu, “Accurate dynamic modeling of twisted string actuators accounting for string compliance and friction,” *IEEE Robotics and Automation Letters*, vol. 5, no. 2, pp. 3438–3443, 2020. doi: 10.1109/LRA.2020.2970651.
- [9] D. Crosby, J. Carrasco, W. Heath, and A. Weightman, “A novel triad twisted string actuator for controlling a two degrees of freedom joint: Design and experimental validation,” in *2022 International Conference on Robotics and Automation (ICRA)*, IEEE, 2022, pp. 11388–11394.
- [10] M. W. Spong, S. Hutchinson, and M. Vidyasagar, *Robot modeling and control*. John Wiley & Sons, 2020.
- [11] F. Dessen, “Coordinating control of a two degrees of freedom universal joint structure driven by three servos,” in *Proceedings. 1986 IEEE International Conference on Robotics and Automation*, vol. 3, 1986, pp. 817–822. doi: 10.1109/ROBOT.1986.1087559.

- [12] *Dc micromotors - precious metal commutation*, Dr. Fritz Fauhaber GmbH & Co. KG, Feb. 2020.
- [13] J. Shigley, C. Mischke, and R. Budynas, *Mechanical Engineering Design* (McGraw-Hill series in mechanical engineering). McGraw-Hill, 2004, ISBN: 9780072520361.



**Damian J. Crosby** is a PhD student in the school of Mechanical, Aerospace and Civil Engineering, University of Manchester, Manchester, U.K. He received a B.Sc. in Special Effects Development from The University of Bolton, U.K., in 2010, and a M.Res. in Robotics from The University of Plymouth, U.K., in 2012. He worked as a Research Technician at The University of Manchester from 2013 to 2017, before commencing his PhD.

- 
**Joaquin Carrasco** is a Lecturer at the School of Electrical and Electronic Engineering, University of Manchester, UK. He was born in Abarn, Spain, in 1978. He received the B.Sc. degree in physics and the Ph.D. degree in control engineering from the University of Murcia, Murcia, Spain, in 2004 and 2009, respectively. From 2009 to 2010, he was with the Institute of Measurement and Automatic Control, Leibniz Universitt Hannover, Hannover, Germany. From 2010 to 2011, he was a research associate at the Control Systems Centre, School of Electrical and Electronic Engineering, University of Manchester, UK.

- 
**William P. Heath** is Chair of Feedback and Control in the School of Electrical and Electronic Engineering, University of Manchester, Manchester, U.K. He received the B.A. and M.A. degrees in mathematics from Cambridge University, U.K., in 1987 and 1991, and the M.Sc. and Ph.D. degrees in systems and control from the University of Manchester Institute of Science and Technology, U.K., in 1989 and 1992, respectively. He was with Lucas Automotive from 1995 to 1998 and was a Research Academic at the University of Newcastle, Australia from 1998 to 2004. His research interests include absolute stability, multiplier theory, constrained control, and system identification.

- 
**Dr. Andrew Weightman** graduated in 2006 with a PhD in Mechanical Engineering form the University of Leeds. Whilst at the University of Leeds he developed rehabilitation robotic technology for improving upper limb function in adults and children with neurological impairment which was successfully utilised in homes, schools and clinical settings. In 2013 he moved to the University of Manchester, School of Mechanical, Aerospace and Civil Engineering as a Lecturer in Medical Mechatronics. Dr Weightman has research interests in biomimetic mobile robotics, rehabilitation robotics, robotics for nuclear decommissioning and collaborative robotics.

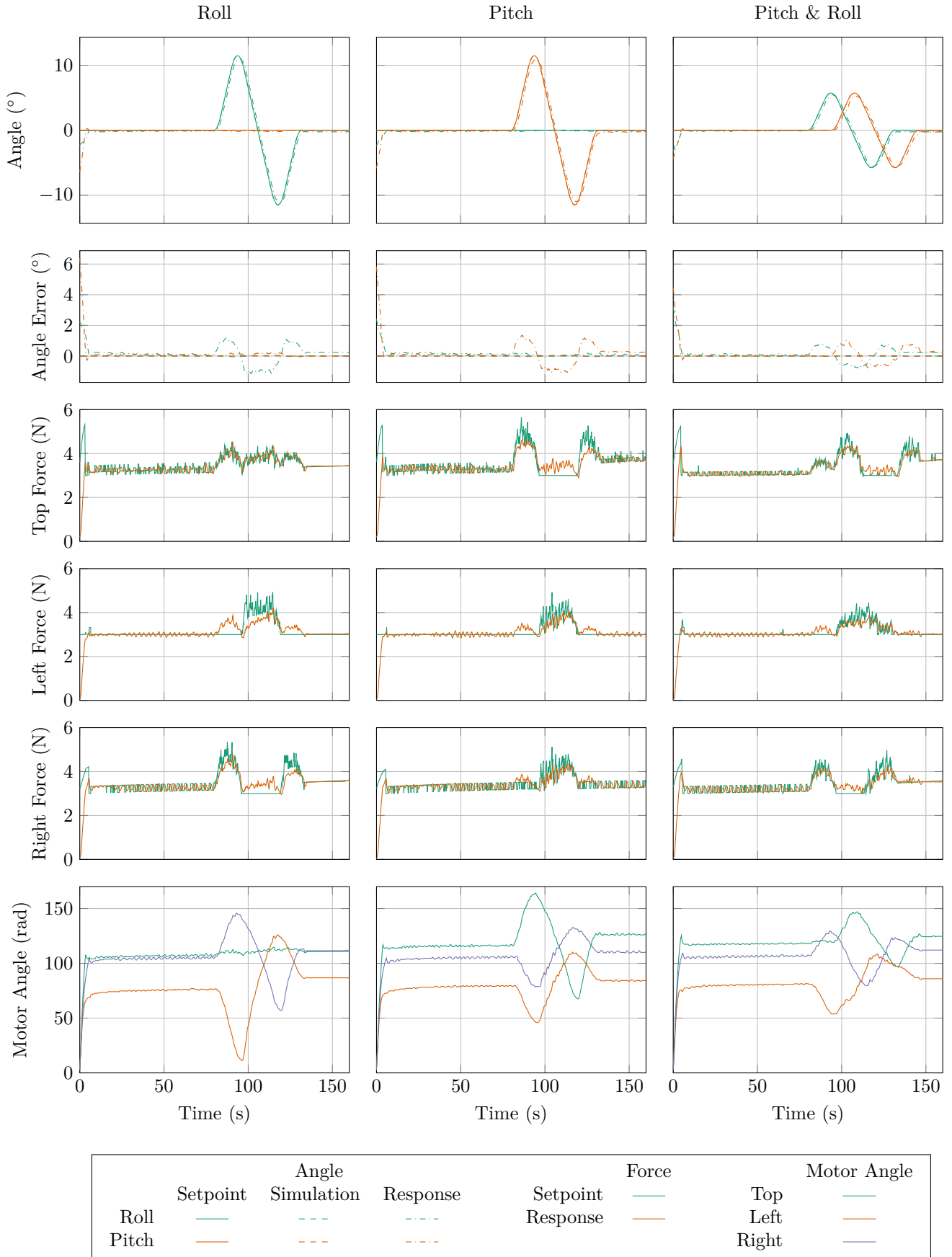


Fig. 13: Plots of the response for three different trajectories, one on only the roll axis  $\theta_1$  (column 1), one on only the pitch axis  $\theta_2$  (column 2), and one on both axes  $\theta_1$  and  $\theta_2$  (column 3). Plots include AUJ orientation, forces at the top, left and right TSA, and the motor positions. Note the simulation error is very small, so the plot cannot be seen on the graph.

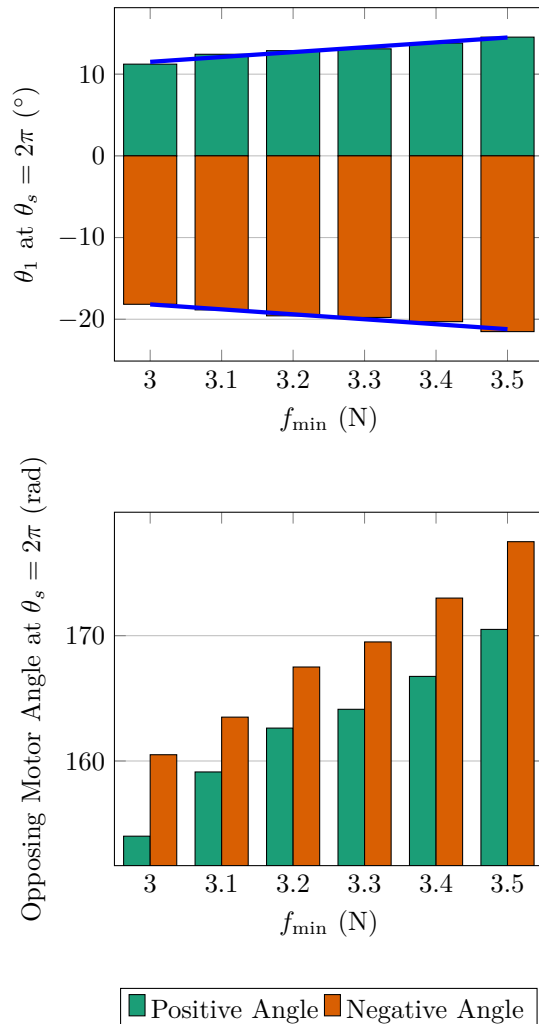


Fig. 14

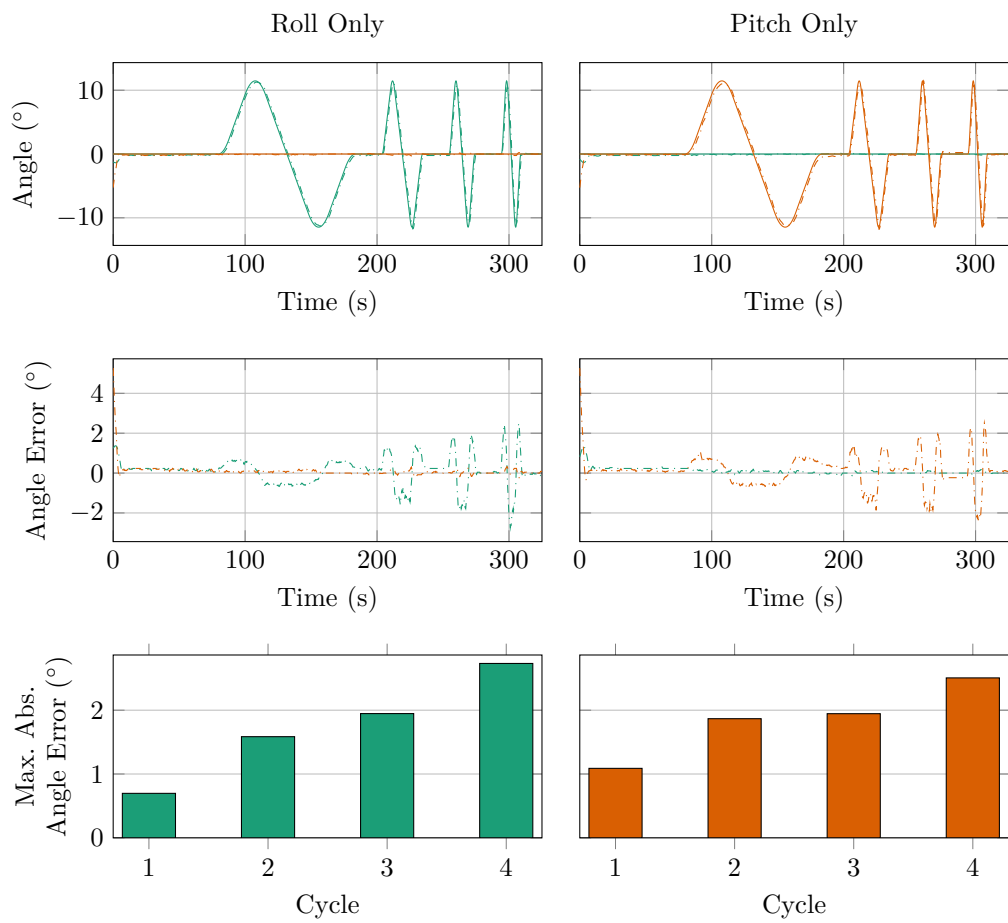


Fig. 15

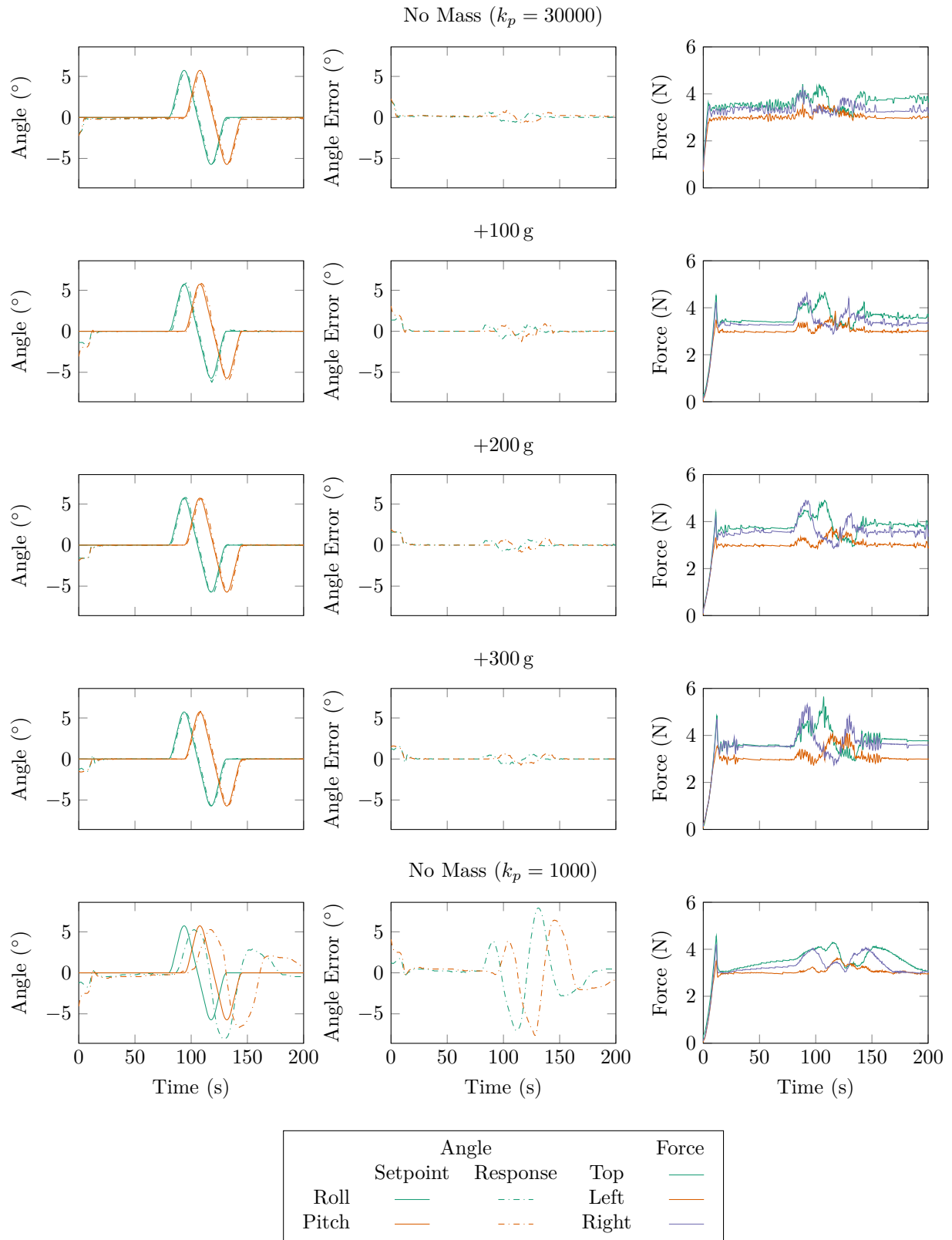


Fig. 16

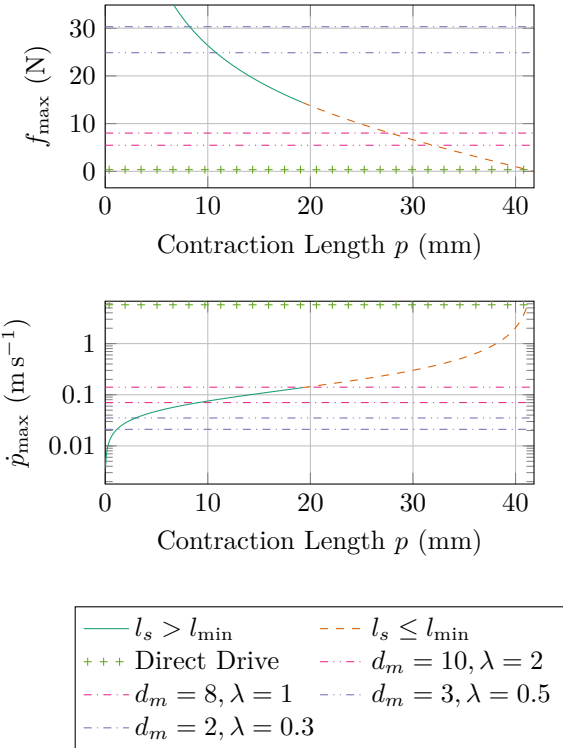


Fig. 17: Performance comparison of the TSA configuration using coefficients from table I to various leadscrew configurations with different  $d_m$  and  $\lambda$ , and the direct drive, where  $\mu = 0.1$  for the leadscrews.

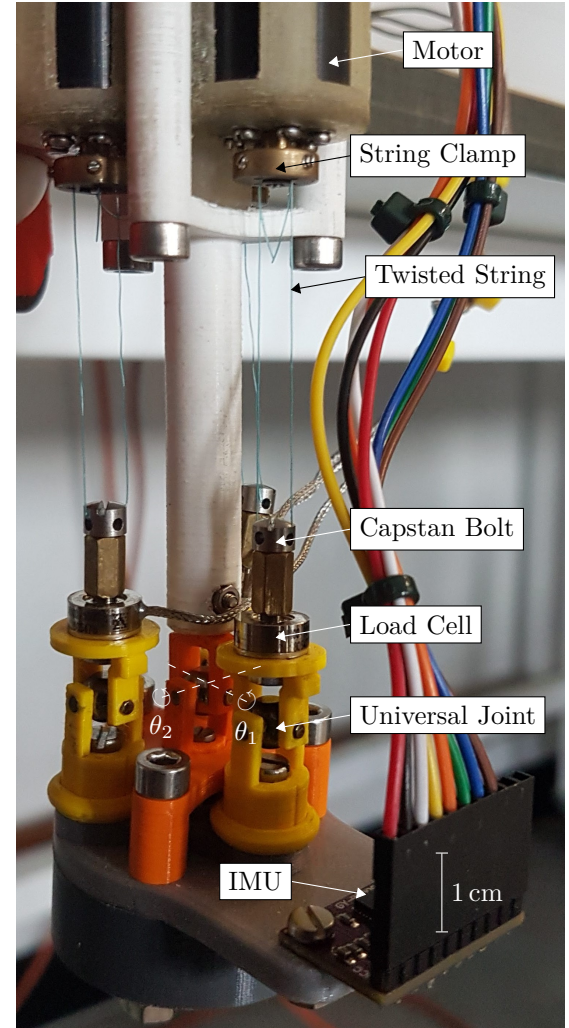
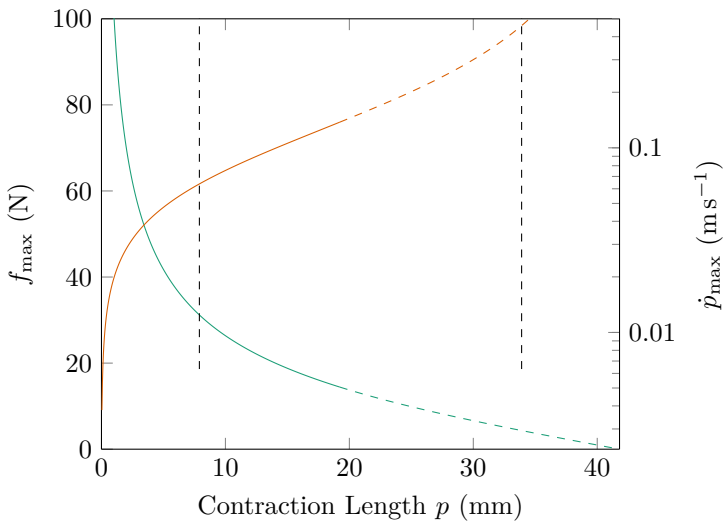
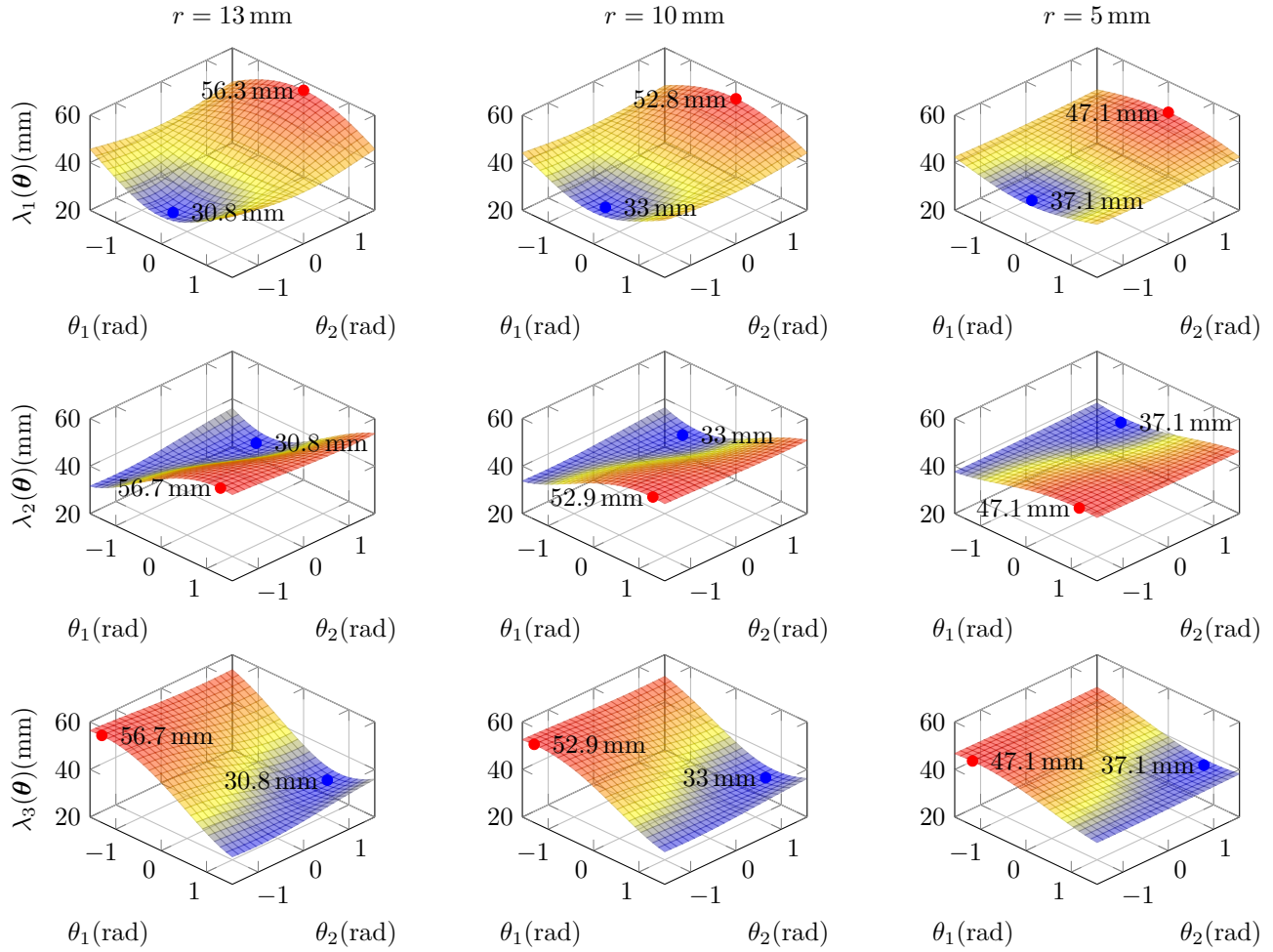


Fig. 18: Annotated photograph of the experimental model, with the roll  $\theta_1$  and pitch  $\theta_2$  axes marked.



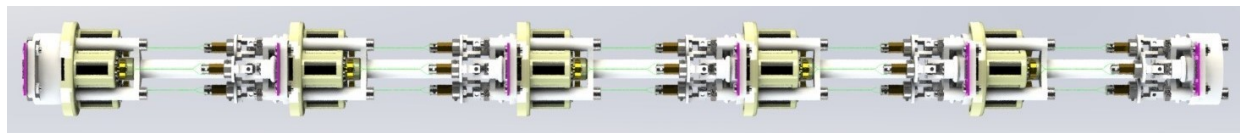


Fig. 19: Visualisation of several TSA AUJ chained together to form a robotic snake or tail.